On the complexity of seismic waves trapped in non-flat geologic features

Domniki Asimaki & Kami Mohammadi
California Institute of Technology, Pasadena CA91125, USA
Department of Mechanical and Civil Engineering

ABSTRACT
Most earthquake engineering and seismological models make the sweeping assumption that the world is flat. The ground surface topography, however, has been repeatedly shown to strongly affect the amplitude, frequency, duration and damage induced by earthquake shaking, effects mostly ignored in earthquake simulations and engineering design. In this talk, I will show a collection of examples that highlight the effects of topography on seismic ground shaking, and I will point out what these results suggest in the context of the current state-of-earthquake engineering practice. Examples will range from semi-analytical solutions of wave propagation in infinite wedge to three-dimensional numerical simulations of topography effects using digital elevation map-generated models and layered geologic features. I will conclude by demonstrating that 'topography' effects vary strongly with the stratigraphy and inelastic behavior of the underlying geologic materials, and thus cannot be accurately predicted by studying the effects of ground surface geometry alone.

1 INTRODUCTION

The term local site conditions refers to the mechanical properties of near-surface geological formations and the geometry of the ground surface and subsurface. Local site conditions can significantly distort the seismic waves that travel from the deeper layers of the crust compared to what the ground motion would have been on the surface of a flat homogeneous linear elastic half-space. This distortion that takes place in the near-surface is referred to as 'site effects', and includes phenomena such as large amplification, frequency content shifts and significant spatial variability of seismic ground motion, all of which are very important for the assessment of seismic risk, in microzonation studies, and in the seismic design of important surficial and subterranean facilities.

Although the problem of seismic wave scattering by topographic irregularities has been studied for several decades in seismology and geophysics, only recently it has attracted the attention of geotechnical earthquake engineering researchers. Topography effects are prominent changes of seismic signals (intensity, frequency content and duration) that systematically take place when seismic waves encounter in their path topographic features (hills, ridges, canyons, cliffs, and slopes); subsurface geologic formations (sedimentary basins, alluvial valleys); and/or geological lateral discontinuities (e.g., ancient faults, debris zones). The effects of the interaction between propagating waves and surface or subsurface irregular geologic features can be dramatic: examples of records that have been attributed in part to topography effects include the PGA=1.93g recording of the hilltop Tarzana station during the 1994 Northridge Earthquake (Bouchon 1973); the Pacoima Dam (PGA=1.25g) recording during the 1971 San Fernando earthquake (Boore 1972a); and the recent extraordinary ground motion (PGA=2.75g) recorded at K-Net station MYG004 on the crest of a 5m high, steep man-made slope during the 2011 Tohoku Earthquake (Nagashima et al. 2014). Extensive review studies that include numerous other examples have been published by Geli et al. (1988), Bard (1999), and Assimaki et al. (2005a).

Observational evidence from past earthquakes indicates that damage concentration occurs where steep slopes or complicated topography are present; buildings located on the tops of hills, ridges, and canyons, suffer more intense damage than those located at the base. There is also strong-recorded evidence that surface topography affects the amplitude and frequency content of the ground motions. Reviews of such instrumental studies and their comparison to theoretical results can be found in Geli et al. (1988), Faccioli (1991), Finn (1991) and Bard (1999). Prompted by observational and instrumented evidence, the problem of scattering and diffraction of seismic waves by 2D idealized topographies on the surface of elastic homogeneous half-spaces has been studied by many researchers (e.g. Boore 1972b, Bouchon 1973, Sánchez-Sesma and Rosenblueth 1979, Sánchez-Sesma 1983,1985,1990). A limited number of studies on complex configurations such as topography with soil layering and/or 3D effects can be found in Bard and Tucker (1985), Ashford et al (1997), Graizer (2009), Assimaki et al (2005b,c) and Assimaki and Jeong (2013).

Numerical and semi-analytical published studies have qualitatively corroborated these observations, but when compared to field recordings, have been shown to systematically underestimate the absolute level of amplification up to an order of magnitude or more in some cases. This discrepancy between theory and observations has been attributed, at least in part, to idealizations of the above studies such as the assumptions of 2D geometry, homogeneous medium, linear elastic response, and monochromatic or narrowband ground shaking.

In this paper, we give an overview of our work in the past 10 years to bridge the quantitative gap between theoretical studies and observations by systematically studying the role of geometry, stratigraphy, and ground motion characteristics through a series of elaborate

numerical analyses. We specifically start from the topographic amplification caused by a 2D infinite wedge on the surface of a homogeneous elastic halfspace, and extend the state-of-the-art understanding of wave focusing and scattering by this fundamental block of irregular ground surface geometries. From there, we gradually increase the geometric and stratigraphic complexity up to a 3D convex layered topographic feature, identifying in each level the controlling factors of topographic amplification. All simulations are performed for linear elastic materials, appropriate to represent the geologic material response to low strain motions. Our results provide new insights into the effects of surface topography and its nonlinear coupling with subsurface soil layering, and suggest that in real conditions, topographic amplification can only be quantitatively captured when geometry and stratigraphy of the site are simultaneously accounted for in theoretical predictive models.

2 INFINITE WEDGE: FIRST ORDER GEOMETRIC COMPLEXITY

Wedge models have been traditionally used in wave propagation studies as fundamental blocks of geometric discontinuities. Typical wedge shaped features that are of interest in various fields of science and engineering include continental margins, mountain roots, and crustal discontinuities in geophysics and seismology; ground surface topographic features in earthquake engineering; and surface defects and cracks in non-destructive testing.

In seismology and geotechnical earthquake engineering, the solution of wedge problem is an important step in understanding the behavior of seismic waves at wedge shaped obstacles. When the incoming seismic wave, which is generated by various mechanisms (e.g. the causative fault), propagates through the medium and hits the wedge-shaped scatterer, its characteristics (e.g. amplitude, frequency and duration) can significantly change because of such geometrical heterogeneity. That is the reason why simple theories cannot adequately explain the recorded wavefield. The wedge solution also helps to describe the scattering of elastic waves from surface topographies with traction free boundary and within dipping layers with mixed boundary conditions. Real surface and sub-surface topographies can first be approximated by simplified convex or concave geometries, and then analyzed as the sum of isolated wedge parts (as a first order approximation).

Let us first consider the initial-boundary value problem of elastic wave scattering by an infinite wedge (Figure 1); we simulate the problem using a finite difference (FD) model, and validate it for amplification of in-plane shear wave at the tip of two wedges (θ = 90° and 120°) using the analytical solution by Sanchez-Sesma (1990).

For these two scenarios, the complete reflection of incident SV waves – mode preserving for 90° and mode converting for 120°– enabled Sanchez-Sesma (1990) to obtain the analytical solution using geometric methods. The velocity time histories at the wedge tip (Figure 2) show the amplification factors of 6e-4 and 4.0006 for 90° and 120° wedges, respectively, which –considering numerical rounding errors and resolution—is exactly equal with the corresponding analytical solutions, namely 0 and 4. Figure 3 shows seismogram synthetics for these two wedge and wave propagation scenarios, and highlights the path of different wave types. As can be seen, the waveforms consist of the incident *SV* wave (*S)* and its specular reflection from the wedge tip (S_1). The waves *S* and S_1 completely satisfy the boundary conditions along the wedge faces, which is why there is no diffracted wave generated at the vertex.

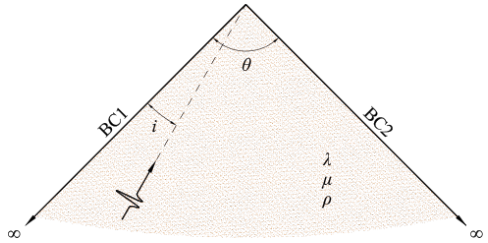

Figure 1. General configuration of the wedge problem

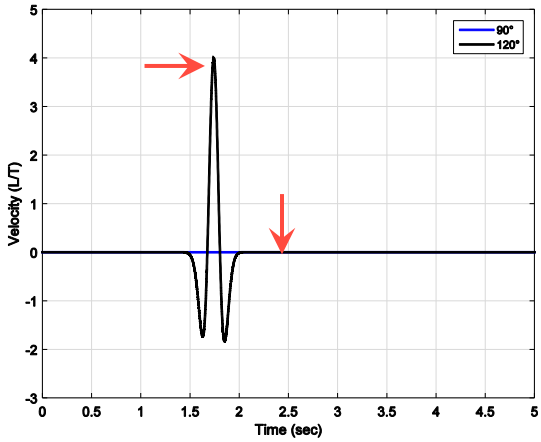

Figure 2. Velocity time history at the tip – 90° and 120° for an incident ground motion with amplitude 1. Note that the free surface response (180°) would have amplitude 2.

After validating the numerical model, we extend the solution to a broader range of internal angles. One of the most interesting cases is the vertically propagated SV wave incident on the wedge face at the critical angle. For Poisson material (v = 0.25), the critical angle of incidence and the corresponding wedge angle (critical wedge angle) are obtained as 35.26° and 109.48°. Beyond the critical angle, the mode converting part of reflection propagates along the wedge face as a surface wave. This is important for our analysis because the maximum tip amplification occurs at this wedge angle. The scattered wavefield of this geometry is more complex because of additional diffracted P, S and surface waves from the tip.

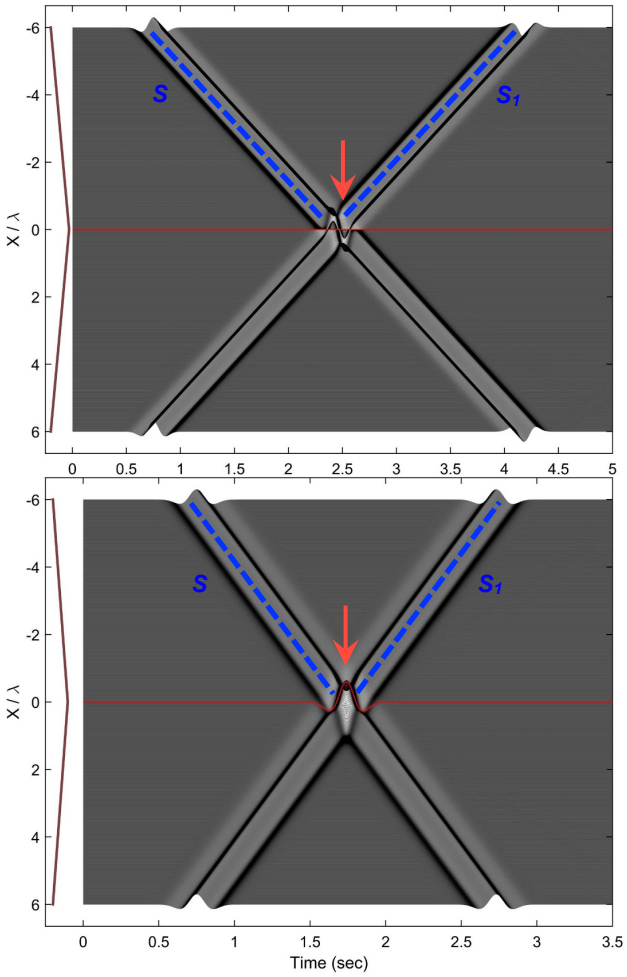

Figure 3. Seismogram synthetics of horizontal velocity – ↑: 90°, ↓:120°. Vertical axis depicts the distance from the crest (X) normalized by the dominant wavelength of the Ricker incident pulse (λ). The wedge geometry is indicated by the brown line next to the vertical axis.

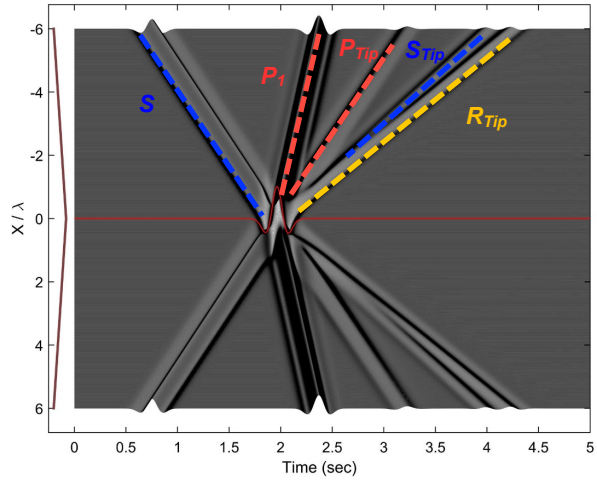

Figure 4. Seismogram synthetics of horizontal velocity – 109° wedge.

Figures 4 and 5 show the seismogram synthetics and wavefield snapshots for the critical wedge. In addition to incident SV wave (path S), there is a complete set of diffracted wavefield from the wedge tip (all components with Tip subscript) as well as a secondary reflected P wave (P_1). The later shows that the compressional part of primary reflection from each face will further reflected from the opposite side. In addition, the slopes of tip-diffracted wave components show their relative velocity as expected. The superposition of surface waves that contain most of the incident wave energy result in such a high peak amplitude (amplification factor of ~13.5 in Figure 6). Different parts of the total scattered wavefield along with the extraordinary large surface motion at tip are better represented in the snapshots.

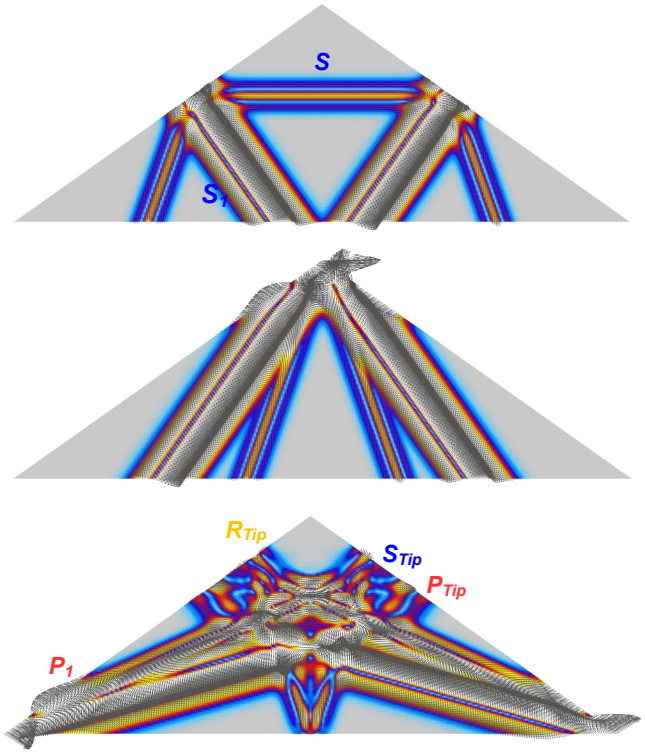

Figure 5. Snapshots of total wavefield – 109° wedge; (top) incident waveform (S) has not encountered the crest yet (time 1.5 sec in Figure 4); (middle) incident waveform arrives at the crest (time 2.0 sec in Figure 4); and (bottom) reflected, refracted and scattered waves travel away from the crest (2.5 sec in Figure 4)

3 2D TOPOGRAPHY

We next increase the geometric complexity of our study on topography effects by adding characteristic (finite) length(s) to the infinite wedge problem, and performing a set of systematic analyses on the resulting idealized feature. The feature is characteristic of a dam (embankment) geometry subjected to vertically propagating Ricker SV wave (Figure 7). For different dimensionless width ζ (normalized by the incident wavelength, D/λ), the problem is divided into three groups, namely a single slope, a wedge and a dam. For each case, we calculate

amplification factors as a function of the slope angle, the dimensionless height (normalized by the incident wavelength, H/λ), and dimensionless width. A sample of our results for the case of slope angle $\alpha = 45°$ is presented in Figure 8.

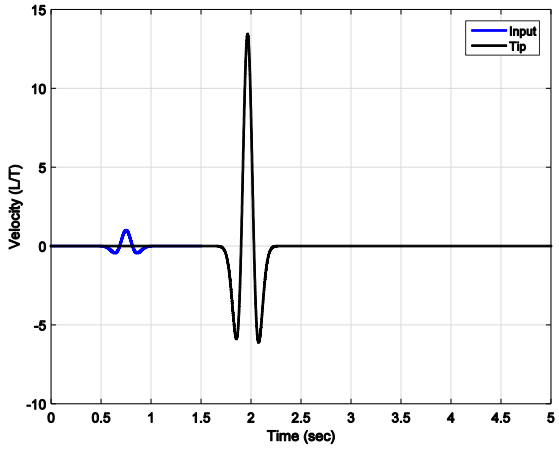

Figure 6. Tip velocity response for critical incidence (incident wave pulse has amplitude 1 and peak response at the wedge crest has amplitude 13.5)

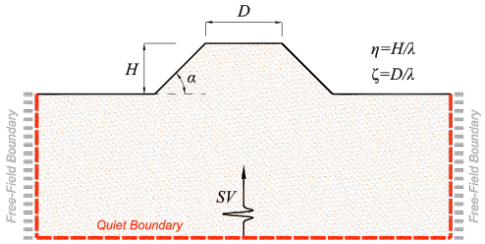

Figure 7. General configuration for 2D topography

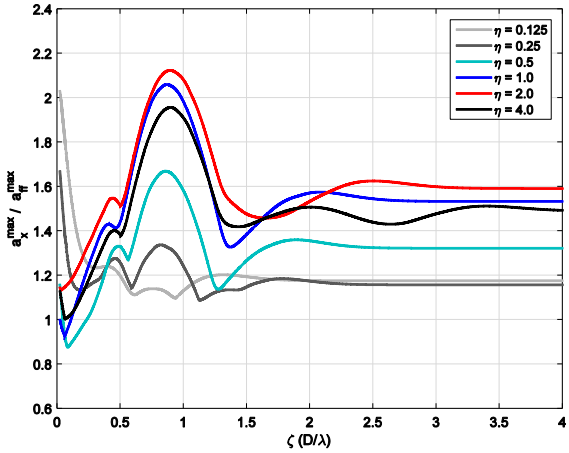

Figure 8. Horizontal amplification factor (vertical axis: ratio of peak response at the crest to incident amplitude) vs. normalized width at different dimensionless heights, which are proxies of different frequencies (slope angle: $\alpha = 45°$)

Note that for the same slope angle, the amplification curves for different dimensionless heights and widths yield similar amplification curves of different amplitude, namely similar waveform patterns. Changing the normalized height, we generally see oscillations of larger amplitude for higher frequencies (for example, moving from gray to red in Figure 8). In other words, the dimensionless height determines whether the incident wave 'see' the topography or not. The normalized width, on the other hand, is related to the interaction of two sides in terms of constructive and destructive interferences. Therefore, we see a wedge and single slope types of behavior for sufficiently small and large dimensionless width, respectively. In between, there may be a couple of peaks and troughs due to the interaction of surface waves. It is noteworthy that the practical large distance, which gives rise to single slope response, is much smaller than the theoretical value ($\zeta \to \infty$). Thus, we can define a threshold distance beyond that the additive effect of either side on the response of other side is negligible.

There are three dimensionless widths where the response of dam topography with $\eta = 1.0$ shows a drastic change (peak and trough), namely $\zeta = 0.88$, 1.38 and 2.09. Seismogram synthetics of horizontal and vertical accelerations are presented for the scenario of maximum amplification ($\zeta = 0.88$) in Figure 9.

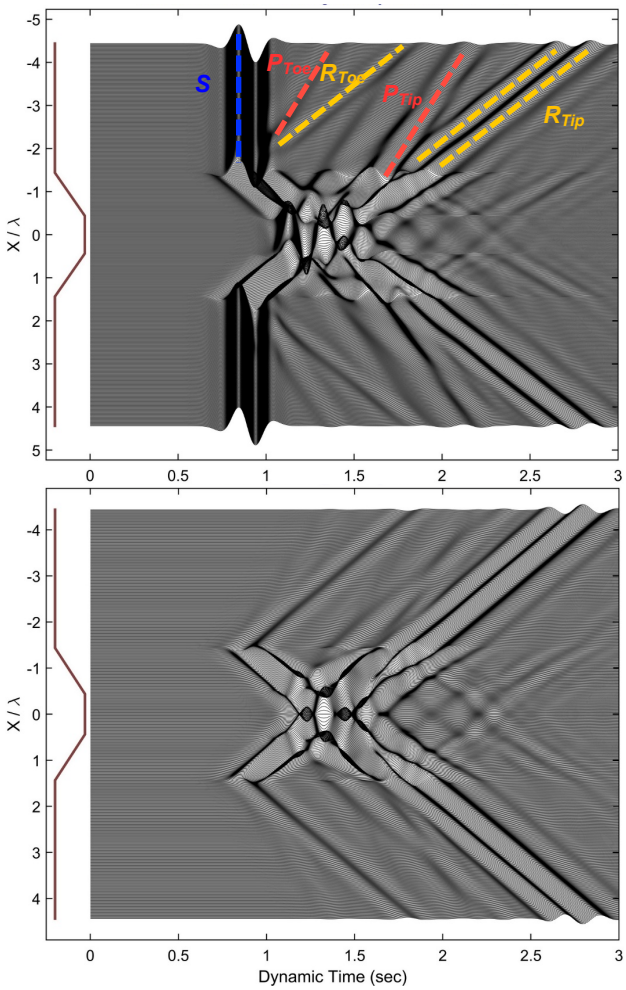

Figure 9. Seismogram synthetics of acceleration for dam (↑: horizontal motion (H), ↓: vertical motion (V)) for $\alpha = 45°$ and $\zeta = 0.88$.

This dimensionless width corresponds to the constructive interference of wavefield components generated from two adjacent slopes and the incident wave. These components comprise of surface Rayleigh and body P, S waves diffracted from the toe and tip of each slope. We can also see the trapping of diffracted body waves in the middle part of dam that gradually leaks to the lower half-space. Snapshots of the total wavefield for the same geometry (Figure 10) provides us with further information about the underlying scattering mechanism. Diffraction of incident shear wave at the toe, constructive interference of wave components at the maximum station, and the trapping of diffracted energy within the feature are clearly shown in Figure 10. Finally, we can see the two-sided effects parameterized by means of the dimensionless width through the spatial variation of amplification factors. Figure 11 shows a sample of such plots for α = 45° dam at three characteristic points of ζ = 0.88, 1.38 and 2.09.

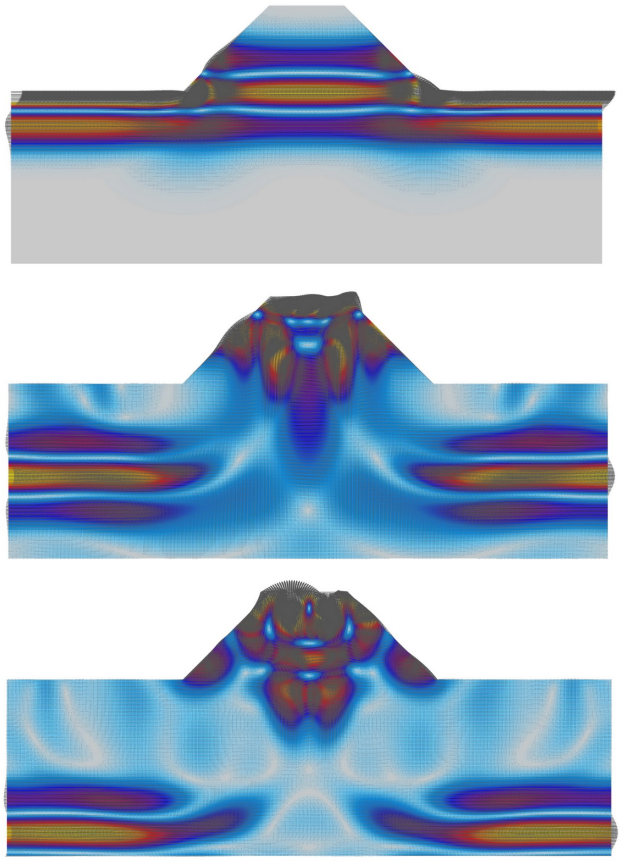

Figure 10. Snapshots of total wavefield – α = 45°, ζ = 0.88. From top to bottom, the figures correspond to times 1.5 sec, 2.0 sec and 2.5 sec.

Increasing the width from the point of maximum amplification (ζ = 0.88) gives rise to a local minimum due to destructive interference. The scattered wavefields generated by two slopes starts to separate if we further increase the width between the crests (as for the case of ζ = 2.09). We should note that while the resultant scattered wavefield is very sensitive to the distance of the crests on the top of the embankment, due to constructive and destructive interference, the amplification curves that generated by the wave diffraction at the toe is practically identical in all three cases, both in spatial distribution and amplification order of magnitude (ranging between amplification 1.0 at the free-field and 1.1 near the toe).

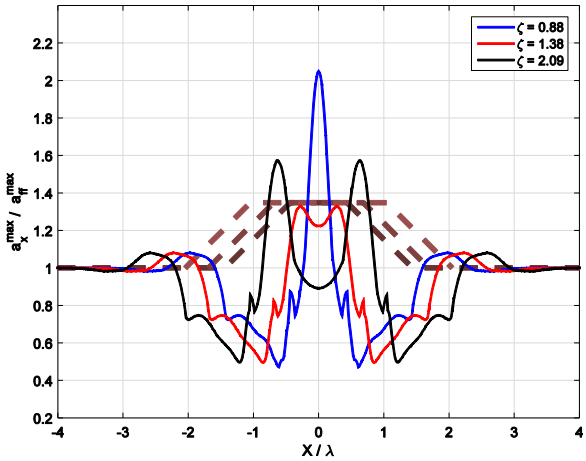

Figure 11. Spatial variation of amplification factor – α= 45°

4 NONLINEAR COUPLING EFFECTS

So far, we looked briefly at the effects of geometric discontinuities, from the simple case of 2D infinite wedge to more complex 2D convex features. The results, which are presented in the form of topography amplification patterns, could be used to explain field observations in a more realistic way. Nonetheless, a complete site response analysis for strong ground motion should also account for the change in material properties.

We next investigate the effect of surface topography when it is combined with subsurface soil stratigraphy as a simple case of material heterogeneity. We systematically investigate the soil-topography coupling effects for the 2D dam-type topography with two different types of near surface layering (Figure 12). Controlling parameters in this case, in addition to the geometric features explained above, are the thickness of upper layer and the stiffness contrast between two layers have been defined in dimensionless form. To study the coupling effect, we compute the variation of horizontal peak amplification with dimensionless width for several combinations of impedance contrast, Q, and normalized thickness of surface layer, ξ (Q is less than unity for near surface soft layer). Figure 13 shows a sample of these results for both layered models with α = 45° and η = 1.0 where the amplification curve of homogeneous model is added for comparison purpose (blue curve). For the layered model with horizontal interface, to which we shall refer as M1, we approach the problem similarly to the case of single layer dam. However, there are two differences between M1 and the original problem. First, the transmitted wave in the top layer carries less energy than the incident wave, depending on the stiffness contrast.

For stiffness ratios considered in this study, the soil amplification (1D site response) controls the overall behavior at the far-field and gives rise to larger amplification factors. Another deviation of M1 from the homogeneous problem is its finite depth (as opposed to the homogeneous halfspace of the previous section). This results in multiple reflections between two layers (the stiffness contrast controls the number of reflections) and higher order diffracted waves (both body and surface) from tips and toes.

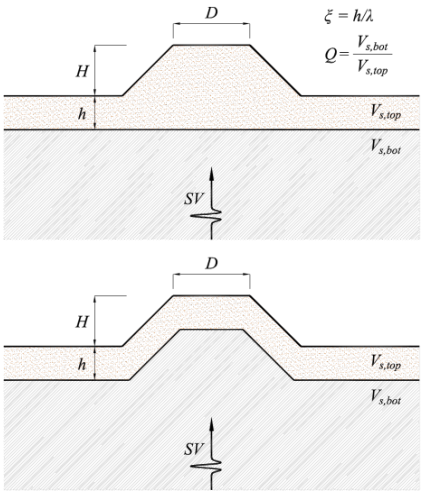

Figure 12. Configurations of layered models used for investigating the coupling effect – (↑: M1, ↓: M2)

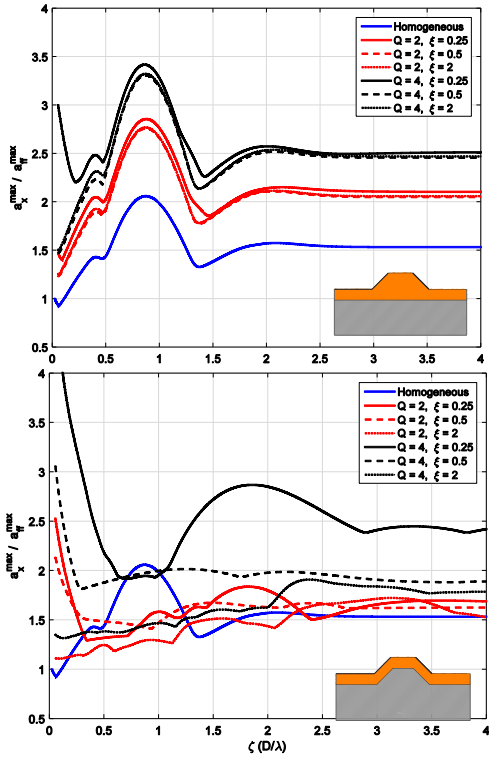

Figure 13. Horizontal amplification factor vs. normalized width for various values of thickness and stiffness contrast

Model M2 on the other hand, with identical topography geometry but with a surface layer of constant thickness instead of a flat interface between soil and rock at depth, creates more sources of scattering (tips and toes of interface) and narrower surface region for trapping the incident energy. This additional complexity results to an even larger number of reflections between two layers as compared to model M1.

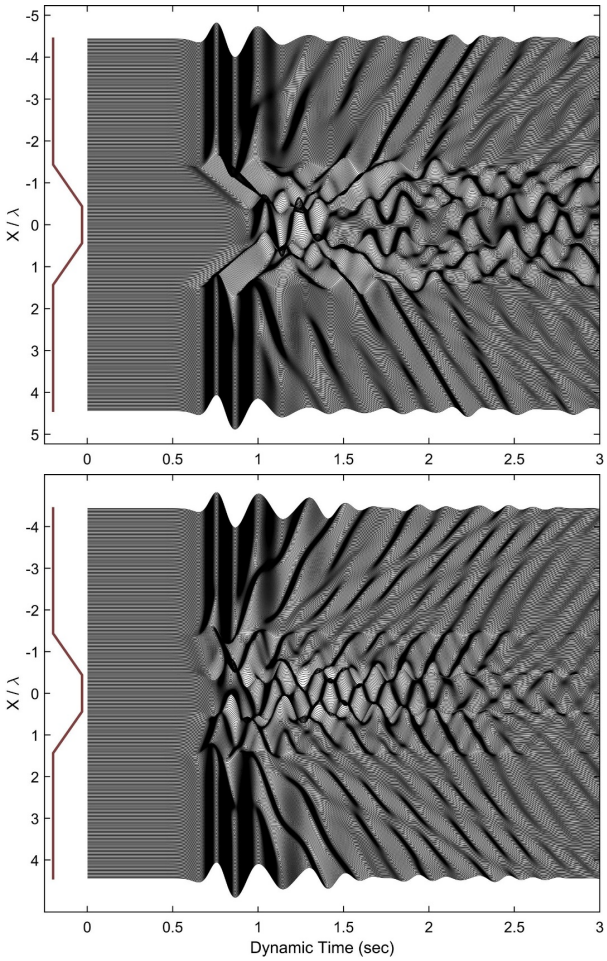

Figure 14. Seismogram synthetics of acceleration (↑:M1, ↓: M2) – ζ = 0.88, ξ = 1/4, Q = 4

For model M1, the amplification curves are similar to that of single layer as expected, since the peak is determined at the first arrival. The main difference lies in the duration and frequency content. Also, the peak amplification factor occurs at the same dimensionless width as in the single layer case (ζ = 0.88). Furthermore, they are clustered in three different categories (black, red and blue) based on the stiffness contrast with higher values at larger contrast. The dimensionless thickness of upper layer, on the other hand, has little effect on the amplification response. This is also expected as the constructive interference of first arrivals (direct and diffracted waves) gives rise to peak amplification. The lower plot of Figure 13 shows a different wave mechanism for model M2. First, they are no longer similar to the single layer model inasmuch as peaks and troughs occur

at different dimensionless widths. In addition, there is no clustering based on stiffness contrast. Instead, the thickness of upper layer play a more important role in the form of amplification curves. One could see that the curves of same line type and different colors are almost similar. This is because the free surface boundary and interface form a single scatterer whose characteristic length (thickness) controls the consequent wavefield. Finally, the threshold dimensionless width, beyond that the dam response turns into that of single slope, is much larger than model M1.

Figure 14 shows the seismogram synthetics of the horizontal ground motion component at the peak width of homogeneous case (ζ = 0.88) for ξ = 1/4 and Q = 4. Model M1 has the same general structure (diffracted surface and body waves from tips and toes on both sides) as that of the halfspace case. The main difference between the two is the reverberation of the body waves in the upper layer, which mask the low amplitude diffracted Rayleigh waves that are prominent in the halfspace case. Model M2 on the other hand has an amplification trough in the normalized width scenario ζ = 0.88 as opposed to M1, and causes a larger number of multiple reflections of body waves because of the shallower sediment depth between two toes, and the increase number of scattering-inducing points.

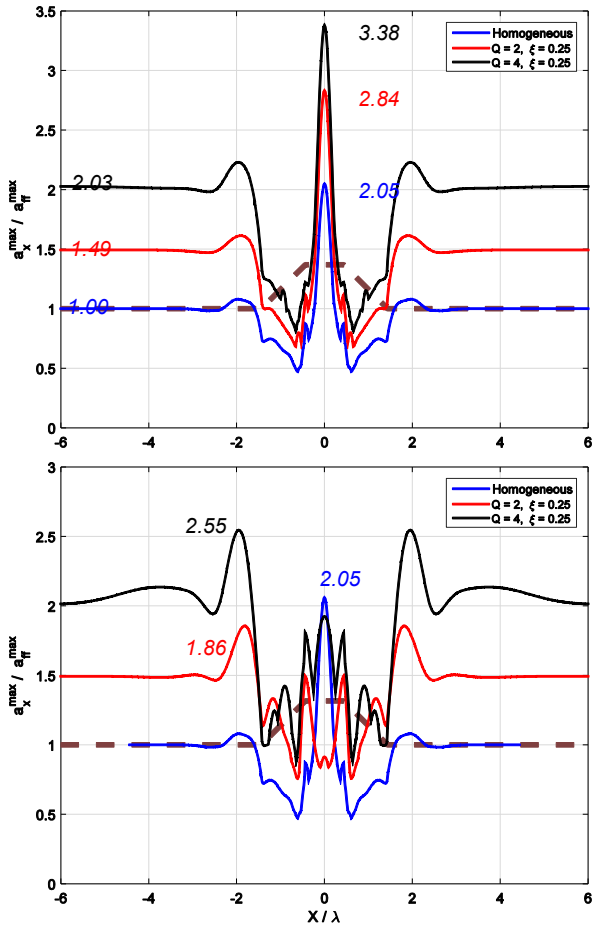

Figure 15. Spatial variation of horizontal amplification factor (↑:M1, ↓:M2) – ζ = 0.88

Figure 15 compares the spatial variation of amplification factor of the two-layered models with the dam model on homogeneous halfspace presented earlier. The nonlinear coupling between soil and topographic amplification can be shown in this figure: the blue curve shows that for this geometry, the topography amplification factor –in absence of soil layers—is 2.05. The red and black curves depict the spatial variation of soil amplification, whose free-field peak amplitude is 1.49 and 2.03 correspondingly for Q = 2 and 4. The amplification factor from soil and topography together is 2.84 and 3.38 for model M1; and 1.86 and 2.55 for model M2, respectively. Had the problem been a pure superposition between the amplification caused by soil and by topography, one would need to scale up the spatial variation curve of the halfspace with the amplification value of the 1D far-field response of the layered structure, to obtain the combined effects of soil and topography. Clearly, this is not the case.

Finally, snapshots of total wavefield for model M2 with ζ = 0.88, ξ = 0.25, and Q = 4 are shown in Figure 16. The top, middle and bottom plots respectively show the initial scattering of incident waves by a surface crust, the maximum amplification that occurs at the two opposite crests, and multiple reflections of energy trapped in the upper layer, respectively.

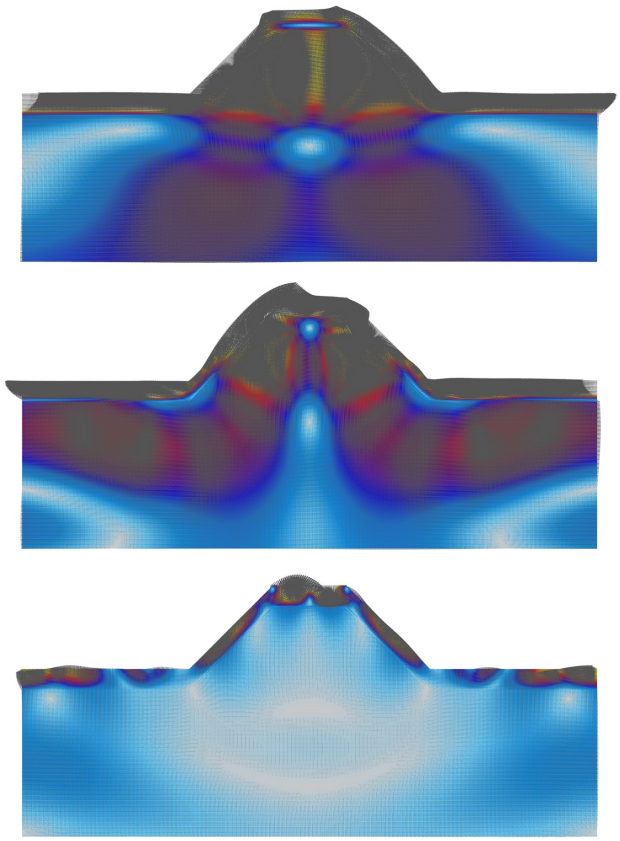

Figure 16. Snapshots of total wavefield for model M2 – *ζ = 0.88, ξ = 0.25, Q = 4*

5 REAL 3D TOPOGRAPHIC FEATURES

To get a better understanding of the complexity of site effects in real cases, we consider a topographic feature near strong motion station CI-LCP in California. Figure 17 shows the bird-eye view of this site along with its topographic map with the strong motion station designated by a yellow triangle. It is clearly seen in the topographic map that the feature is not symmetric with respect to the azimuth angle. To describe the effects of topography in this case, we define two major axes (based on the geometry and expected wave focusing) and subject the feature to incident shear waves polarized in these two directions. We used DEM data of 1/3 arc-second resolution to construct the 3D surface of topographic map. Due to lack of detailed information about the spatial distribution of the stratigraphy, we assumed each a near surface layer with a constant depth. Assuming elastic linear material, we extracted the properties of the various layers in our analysis from Yong et al. (2013) and we list them in Table 1. Along with the layered model, we also consider a homogeneous case to use as benchmark for pure topography effects.

Figures 18 and 19 show the amplification factor maps overlaid by topography contour lines of 5m interval for the homogeneous and layered cases respectively. The amplification factor is defined as the ratio of peak ground acceleration of each point relative to the peak amplitude of the homogeneous model at free-field (FF). Values of peak and free-field amplification factors are also shown on each plot for reference.

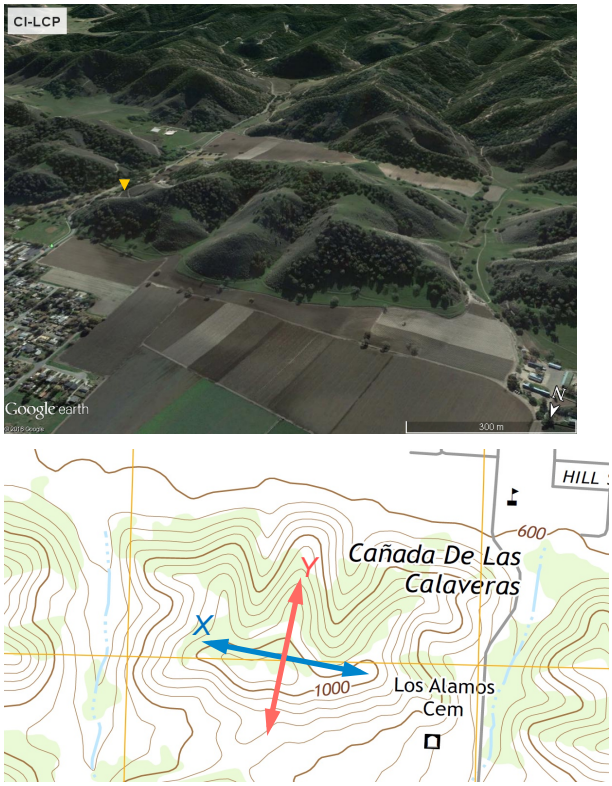

Figure 17. CI-LCP site (↑: bird-eye view, ↓: topo. map)

Since the feature is relatively symmetric with respect to the azimuth angle, we see a little difference between amplification factors/patterns of X and Y polarization scenario for homogeneous model. However, it is still evident that vertical/horizontal ridges are more amplified by X/Y polarized input motion (lines A, B and C vs. lines D and E). Larger amplification is observed at the intersection of horizontal and vertical ridges. The amplification pattern is consistent with the pure topographic effects i.e. amplification/de-amplification in convex/concave regions. Nevertheless, the presence of adjacent topographies and the added complexity of amplification and de-amplification regions is evident. As we can see in Figure 19, however, removing the soil amplification contribution leads to a counter-intuitive distribution of ground motion amplitude, where the peak amplification occurs along canyons and the maximum de-amplification along the ridges.

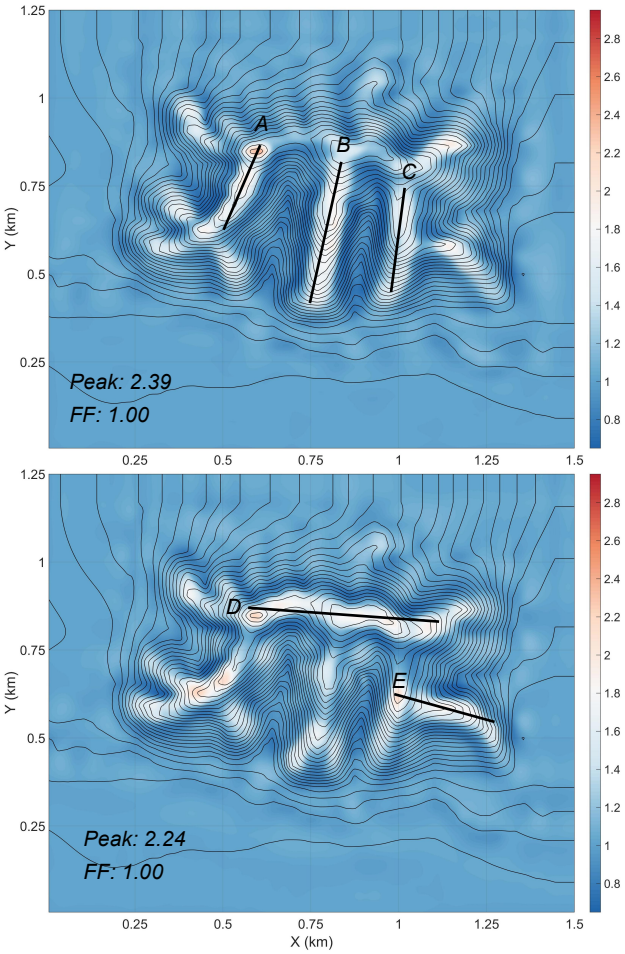

Figure 18. Amplification factor for homogeneous case – ↑: X, ↓: Y polarization

Table 1. Thickness and material properties for different layering scenarios – site CI-LCP

Layering Scenario	Layer	Thick. (m)	V_S (m/s)	ν	ρ (kg/m^3)
Homogeneous	1	---	486	0.333	2000
True Layering	1	7	179	0.333	1800
	2	17	255	0.333	1870
	3	>2λ	486	0.333	2000

Furthermore, the top soft layers, which has an adequate thickness compared to the incident wavelength, plays a decisive role in the overall amplification pattern. Again, the amplification factors of the layered models demonstrate the nonlinear coupling effect of soil layering amplification and topographic focusing and scattering effects. For example, while the 1D site response of the layered structure yields 80% peak amplification (1.80) relative to the homogeneous case, the 3D amplification is only magnified by 33% (2.98) for in the case of the Y-polarized motion, and less so for the X-polarized motion.

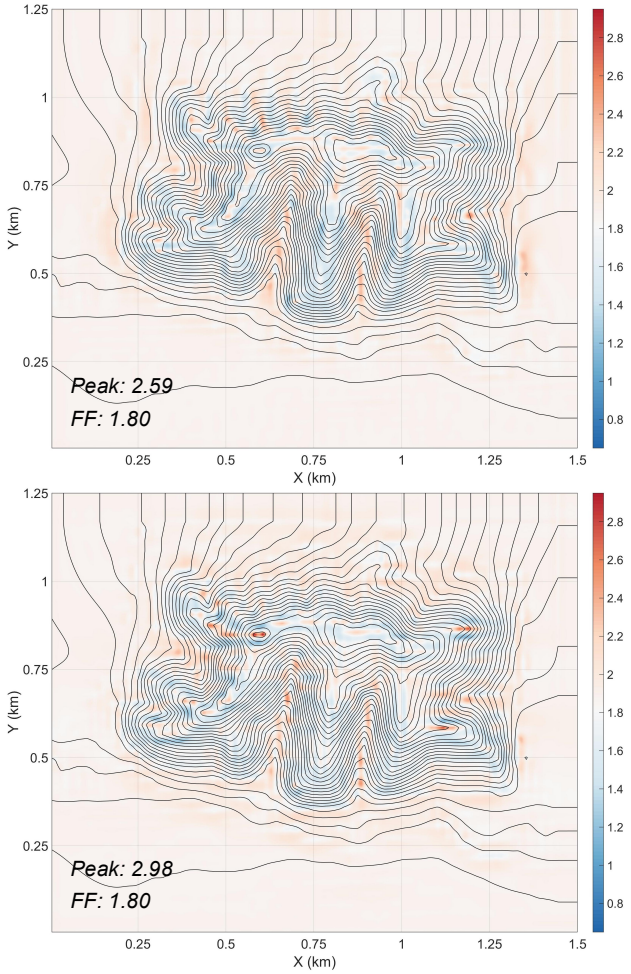

Figure 19. Amplification factor for layered case – ↑: X, ↓: Y polarization

6 CONCLUSIONS

In this study, we gave an overview of our systematic analysis on the key parameters governing the problem of topographic amplification. We started from the topographic amplification caused by 2D infinite wedges on the surface of a homogeneous elastic half-space, and extended the understanding of wave focusing and scattering by this fundamental block of irregular ground surface geometries. From there, we gradually increased the geometric and stratigraphic complexity up to a real 3D layered topographic feature.

Amplification response of the infinite wedge does not depend on the frequency of excitation because it involves no characteristic length. Nonetheless, the wedge angle determines how various wave components i.e. the incident wave, surface waves travelling towards the apex, geometric elastodynamic part, and a set of tip diffracted wavefields interact with each other. Adding an explicit characteristic length in 2D topographies, we introduced further constraints on the wave interference pattern, which in turn, gave rise to a more complex scattered wavefield and amplification patterns. This became even more involved when we replaced the homogenous halfspace with a layered medium that can trap the incident energy, and introduce further scattering.

The most important finding of our work is that the causative factor of what is frequently referred to as topographic amplification is not the ground surface geometry alone, but instead the nonlinear coupling of geometry and underlying soil stratigraphy that affects the amplitude, frequency, duration and direction of wave propagation, even if the underlying soil behavior is linear. Our findings have significant implications that we expect to see precipitating to extreme ground motion predictions; parameterization of ground motion prediction equations; and physics-based simulated ground motions and hazard maps, which should revisit, parameterize and simulate 3D site effects in a way that integrates site, topography and coupling effects thereof.

7 ACKNOWLEDGMENTS

Partial support for this research has been provided by the National Science Foundation under grant award CMMI-0936543 and by the United States Geological Survey under grant award USGS G14AP00064. This support is gratefully acknowledged.

8 REFERENCES

Ashford S.A., Sitar N., Lysmer J. & Deng N. (1997). Topographic Effects on the Seismic Response of Steep Slopes, *Bulletin of the Seismological Society of America*, 87(3), 701-709.

Ashford, S. A., and Sitar, N. (1997). Analysis of topographic amplification of inclined shear waves in a steep coastal bluff, Bull. Seismol. Soc. Am. 87, 692–700.

Assimaki D., Gazetas G. and Kausel E. (2005a). Effects of local soil conditions on the topographic aggravation of seismic motion: Parametric investigation and

recorded field evidence from the 1999 Athens Earthquake, Bulletin of the Seismological Society of America, 95(3)

Assimaki D., Kausel E. and Gazetas G. (2005b). Wave propagation and soil-structure interaction on a cliff crest during the 1999 Athens Earthquake, Soil Dynamics and Earthquake Engineering, 25(7-10), 513-527

Assimaki D., Kausel E. and Gazetas G. (2005c). Soil-dependent topographic effects: A case study from the 1999, Athens Earthquake, Earthquake Spectra, 21(4), 929-966

Assimaki D. and Jeong S. (2013). Ground motion amplification observations at Hotel Montana during the M7.0 2010 Haiti Earthquake: Topography or soil amplification?, *Bulletin of the Seismological Society of America*, 103(5), 2577–2590.

Bard P.-Y. (1982). Diffracted waves and displacement field over two-dimensional elevated topographies, *Geophys. J. R. Astr. Soc.*, Vol. 71, 731-760.

Bard, P. Y. (1999). Local effects on strong ground motion: Physical basis and estimation methods in view of microzoning studies, *Proceedings, Advanced Study Course on Seismotectonic and Microzonation Techniques in Earthquake Engineering* 4, Kefallinia, Greece, pp. 127–218.

Bard, P. Y., and B. E. Tucker (1985). Ridge and tunnel effects: comparing observations with theory, Bull. Seism. Soc. Am. 75, 905–922.

Boore D.M (1972b). Note on the effect of topography on seismic SH waves, *Bulletin of the Seismological Society of America*, 62, 275-284.

Boore, D.M. (1972a). Finite difference methods for seismic wave propagation in heterogeneous materials, In: B.A. Bolt (Editor), Methods in Computational Physics1, 1. Academic Press Inc., NY, pp. 1-37.

Bouchon M. (1973). Effect of topography on surface motion, *Bulletin of the Seismological Society of America*, 63, 615-632.

Faccioli E. (1991). Seismic amplification in the presence of geological and topographic irregularities, *Proceedings of the 2nd International Conference on Recent Advances in Geotechnical Earthquake Engineering and Soil Dynamics*, March 11-15, St Louis, Missouri, Vol. 2, 1779-1797.

Finn W.D.L. (1991). Geotechninal engineering aspects of seismic microzonation, *Proceedings of the 4th International Conference on Seismic Zonation*, August 25-29, Stanford, California, Vol. 1, 199-250.

Geli L., Bard P.-Y. & Jullien B. (1988). The effect of topography on earthquake ground motion: a review and new results, *Bulletin of the Seismological Society of America*, Vol. 78, 42-63.

Nagashima, F., Matsushima, S., Kawase, H., Sánchez-Sesma, F. J., Hayakawa, T., Satoh, T., & Oshima, M. (2014). Application of horizontal-to-vertical spectral ratios of earthquake ground motions to identify subsurface structures at and around the K-NET site in Tohoku, Japan. *Bulletin of the Seismological Society of America*, *104*(5), 2288-2302.

Sánchez-Sesma F.J. (1983). Diffraction of elastic waves by three-dimensional surface irregularities, *Bulletin of the Seismological Society of America*, Vol. 73, 1621-1636.

Sánchez-Sesma F.J. (1990). Elementary solutions for the response of a wedge-shaped medium to incident SH and SV waves, *Bulletin of the Seismological Society of America*, Vol. 80, 737-742.

Sánchez-Sesma, F. J. (1985). Diffraction of elastic SH waves by wedges, *Bull. Seismol. Soc. Am.* 75, 1435–1446.

Sánchez-Sesma, F. J., and E. Rosenblueth (1979). Ground motion at canyons of arbitrary shape under incident SH waves, *Int. J. Earthquake Eng. Struct. Dyn.* 7, 441–450.

Yong, A., Martin, A., Stokoe, K., & Diehl, J. (2013). *ARRA-funded V S30 measurements using multi-technique approach at strong-motion stations in California and central-eastern United States* (No. 2013-1102). US Geological Survey.